J. Fluid Mech. (2006), *vol.* 552, *pp.* 229–256.
doi:10.1017/S0022112006008676 Printed in the United Kingdom

Stratified propelled wakes

By PATRICE MEUNIER† AND GEOFFREY R. SPEDDING

Department of Aerospace and Mechanical Engineering,
University of Southern California, Los Angeles, CA 90007, USA

(Received 22 December 2004 and in revised form 12 October 2005)

This paper presents experimental results on the wake of a propelled bluff body towed at a constant horizontal speed in a linearly stratified fluid. Three regimes of the wake have been found, depending on the angle of attack and on the ratio of drag force to propeller thrust. Most of the experiments were obtained in a first regime where a strong momentum flux is created in the wake, which can be oriented backward or forward depending on the ratio of drag force to thrust of the propeller. The velocity amplitude, wake width and Strouhal number of the wake can be predicted by defining a momentum thickness based on the drag coefficient of the bluff body and the thrust of the propeller. A second regime is obtained for a narrow band of towing velocities, with a relative width of 4%, in which the momentum flux is found to vanish. The wake is characterized by the velocity fluctuations; the scaling exponents of the velocity, vorticity and width of the wake are measured. A third regime is obtained for wakes with a small angle of attack, with a null momentum flux. The mean profile of the wake is found to be asymmetric and its amplitude and wake width are measured. Finally, the relevance of these results to the case of a real self-propelled bluff body is discussed. The presence of weak internal waves or of weak fluctuations of background velocity would lead to a wake in the regime with momentum flux, and would allow prediction of the amplitude, width and Strouhal number of the wake.

1. Introduction

1.1. *Towed-body wakes*

Over a range of intermediate scales (1–100 m in the ocean, 100–1000 m in the atmosphere) geophysical flows are strongly influenced by the background density gradient, giving rise to numerous complex and interesting flow phenomena and numerous problems for large-scale modelling efforts for which these complex processes must appear as single coefficients modelling subgrid-scale processes. One of the canonical problems receiving much attention has been the decay of initially turbulent motions in a stably stratified environment. The review articles by Lin & Pao (1979) and Riley & Lelong (2000) indicate the range of theoretical, numerical and experimental approaches and progress over the years.

One such general problem involving decaying stratified turbulence is the bluff-body wake at moderate and high Reynolds number, which also has certain practical applications. The wakes of towed spheres are characterized by the persistence of large coherent structures, even at high internal Froude number when such order might not be expected to emerge and/or survive to late times (Lin & Pao 1979; Chomaz,

† Current address: Institut de Recherche sur les Phénomènes Hors Équilibre, UMR 6594 CNRS/Universités Aix-Marseille, 49 rue F. Joliot-Curie, F-13384 Marseille Cedex 13, France.

Bonneton & Hopfinger 1993; Spedding, Browand & Fincham 1996; Spedding 1997). Stratified fluids support internal wave motions and the waves emitted by both body and wake have been studied in experiment and theory (Gilreath & Brandt 1985; Bonneton, Chomaz & Hopfinger 1993; Spedding *et al.* 2000; Voisin 1991). Since the coherent wake structures organize in a very ordered fashion (resembling a von Kármán street), the pattern of wave packets emitted by them reflects that order. Indeed if one characteristic were to be specified as diagnostic it is likely to be the coherent structures themselves, and Spedding (2002) proposed that the spacing and lengthscales of these structures, which could be rescaled over all experimentally accessible Reynolds and Froude numbers, could be viewed this way. Voropayev & Smirnov (2003) argued similarly based on experiments on low-Reynolds-number jets in stratified fluids, deriving the same scaling law based on the momentum flux from the jet source.

1.2. *Computations and generalization*

If all towed-sphere wakes are similar in mean and turbulent length and velocity scales, and if the same scaling laws could be derived for objects that were not spheres (essentially point momentum sources), then it seems plausible that the observed characteristics are quite general and applicable to many cases of decaying flows in a stratified fluid (Spedding 1997). It is reasonable to enquire whether the body geometry has any influence at all in the far wake, and Meunier & Spedding (2004) showed that all late wakes with a momentum defect can be rescaled by the momentum flux, regardless of body geometry, for bluff, streamlined and sharp-edged bodies. As a practical matter, the appropriate scaling can be looked up from published drag coefficients for the different body shapes in non-stratifed flows.

The unimportance of initial conditions can also be inferred from the successful simulation of the stratified wake by DNS (Gourlay *et al.* 2001) and LES computations (Dommermuth *et al.* 2002; Diamessis, Domaradzki & Hesthaven 2005) where there is no body, only a mean profile with turbulence superimposed upon it as a starting condition for the flow. The simulations clearly show the emergence of the large-scale (in the horizontal) coherent structures from the initially turbulent initial condition. In the absence of the background density gradient, the same simulation conditions show no emergent coherence.

1.3. *Momentumless wakes*

It seems then that all drag wakes can be treated similarly. However, another class of application concerns the motion and disturbance field of underwater vehicles of various types, and in this case, since they are self-propelled, the drag is balanced by a local thrust, and the wake has no net momentum. The towed-sphere wake, where turbulence production is due to the mean shear, might after all be a special case, not only for naval applications, but also in geophysical flows, where different turbulence production mechanisms may also have, at least on average, zero net momentum.

Indeed, if one searches analytically for similarity solutions, as in Tennekes & Lumley (1972), Finson (1975) and Hassid (1980), then one finds scaling exponents for growth of lengthscales and decay of mean and turbulence quantities that differ significantly from the drag wake case. Using only the simplest eddy viscosity approximation, for example, Tennekes & Lumley (1972) find that while axisymmetric wakes with momentum show mean centreline velocities, $U_W \sim x^{-2/3}$, and wake thickness, $l_W \sim x^{1/3}$, the solutions for the momentumless case are $U_W \sim x^{-4/5}$, and $l_W \sim x^{1/5}$. Finson (1975) notes how the self-propelled wake represents a singular situation, requiring closure approximations in higher-order turbulence quantities. Since production is no longer

driven by a mean shear, it decays rapidly and does not balance the dissipation. Consequently the far wake never becomes independent of initial conditions.

It may not be unrelated that the literature on experimental results is characterized by some degree of scatter (Schooley & Stewart 1962; Naudascher 1965; Swanson, Schetz & Jakubowski 1974; Chieng, Jakubowski & Schetz 1974; Lin & Pao 1974; Schetz & Jakubowski 1975; Lin & Pao 1979; Higuchi & Kubota 1990; Sirviente & Patel 1999, 2000*a*, *b*, 2001) as a wide variety of geometries and mechanisms for production of the momentumless condition have been used. Higuchi & Kubota (1990) in particular noted that the matched case of exact zero-momentum was different in both mean and turbulence decay rates (they were significantly higher) and that a sensitivity to initial conditions (degree of wall roughness) could be detected down to $x/D \simeq 40$–100.

With the exception of Schooley & Stewart (1962), Lin & Pao (1974) and Lin & Pao (1979), none of the momentumless wakes have been in stratified conditions and none have been studied at truly late times. The stratified sphere data of Spedding *et al.* (1996), for example, extends to equivalent $x/D \geqslant 4000$. For most other studies, $x/D \leqslant 40$–100. In stratified fluids, evolution times are expressed in units of buoyancy frequency, N, and the data of Lin & Pao (1979) extend to $Nt \leqslant 60$, compared with $Nt \simeq 3000$ in Spedding *et al.* (1996). Focusing on the late-wake behaviour is not simply an experimental expedient; it also avoids some of the confusion that results when different wakes have different relaxation times to their asymptotic state, which may only be observable very far downstream, as noted by Johansson, George & Gourlay (2003).

Asymptotic theories for far wakes in both momentum and zero-momentum cases have been given by Smirnov & Voropayev (2003) and Afanasyev (2004) but make no statement on the appropriate form of the initial condition (in this case the distribution of localized force doublets) and contain no notion of turbulence modelling. However, such numerical modelling has been done recently by Chernykh, Demenkov & Kostomakha (2001) and Chernykh, Ilyushin & Voropayeva (2003).

1.4. *Objectives*

There is, therefore, considerable uncertainty concerning the extension of previous results from stratified, towed-body wakes to practical applications. Based on available theoretical and experimental work, one would not expect similar scaling laws to apply to either mean or turbulence quantities in the momentumless wake, and one might also not expect the same insensitivity to details of the initial conditions. Currently, there are no quantitative measurements to check these ideas for late wakes in stratified flows. The objective of this paper is to measure wakes at, or close to, the self-propelled point, under the same conditions as for the existing towed-body experiments. The parameters varied will allow systematic investigation of the effect of the strength of the background density gradient, the degree of thrust/under-thrust from the propeller, and the shape of the solid body. The results will be compared for consistency, or lack thereof, with the existing literature, and the relevance of such results to practical flows will be re-examined.

2. Experiment and data analysis

2.1. *Experimental devices*

The materials and methods are similar to those described in detail in Spedding *et al.* (1996). A bluff body with diameter $D \approx 3$ cm is towed at a velocity U_B along the

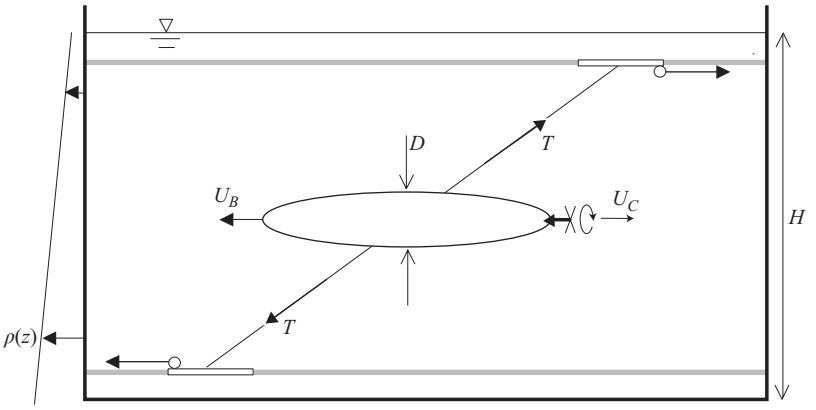

FIGURE 1. Experimental set-up.

x-direction, in a water tank with horizontal dimensions $380 \times 244\ \mathrm{cm}^2$. The bluff body is maintained by three thin wires ($d = 250\ \mu\mathrm{m}$) under strong tension T, as shown on figure 1. These tow wires slide along three guide cables with a minimum of vibration, up to a tow speed of $1\ \mathrm{m\ s}^{-1}$. The disturbances created by the wakes of the tow wires themselves (where $Re < 250$) are negligible in amplitude compared with the wake of the bluff body. Furthermore, the obliquely mounted wires do not intersect the measurement plane, which is at mid-body height in all experiments reported here.

The bluff body has a small propeller made of two flat plates with diameter close to 1 cm, which are fixed to a rotating axis with an angle of roughly 30° to the tow axis. When the propeller rotates, some momentum is expelled backwards, which creates a thrust on the bluff body. However, this does not change the velocity of the bluff body which is fixed through the towing wires. The propeller axis is rotated by a motor located inside the body, whose power comes from an external DC current generator. The current is stopped when the body reaches the end of the tank, to prevent a strong jet created by the propeller from impinging back upon the flow.

Two different bluff bodies have been studied, so the influence of the shape of the object can be determined. The first is a cylinder with diameter $D = 3.35$ cm and length of 15.6 cm. The sharp edges and the non-profiled shape create a very turbulent wake. The second object is a prolate spheroid with diameter $D = 2.54$ cm and length of 15.2 cm. The streamlined object creates a very weakly turbulent wake, and the comparison between these two different body types – streamlined and sharp-edged – can represent a range of possible initial conditions. The boundary layer remained laminar since it was not tripped.

The tank is filled with stably stratified salt water, whose linear density gradient creates a buoyancy frequency $N = (-g/\rho_0)^{1/2}(\partial\rho/\partial z)^{1/2} \approx 2\ \mathrm{rad\ s}^{-1}$. The water depth, $H = 26$ cm, is large compared to the diameter of the bluff bodies $D \approx 3$ cm, and will be considered infinite for the centreplane measurements described. Systematic variation of D/H in Spedding (1997) showed no dependence for such values.

The flow is analysed by measuring horizontal two-dimensional instantaneous velocity fields using particle image velocimetry. For flow seeding, small polystyrene beads with a mean diameter 600–800 μm are carefully sorted in an auxiliary tank to select a density of $\rho_{\mathrm{part.}} = 1.0510 \pm 0.0008$. When introduced in the stratified fluid, the particles settle at the specific height where the fluid has the same density $\rho_{\mathrm{part.}}$, marking an isopycnal with a thickness $\Delta z \approx 3$ mm. The height of the isopycnal can

be modified, by adding or removing small amounts of heavy fluid at the bottom of the tank, so that it is located precisely at the mid-height centreplane of the bluff body. The particles are illuminated by four 1 kW floodlights and their positions are recorded on a Pulnix TM9701 CCD camera positioned above the tank, over a field of view with dimensions $79 \times 56\,\mathrm{cm}^2$. The digital images are treated by a variant of the customized Correlation Image Velocimetry (CIV) algorithm described in detail in Fincham & Spedding (1997). At each grid point, the cross-correlation peak is estimated by a least-squares fit of a function constructed from an average of the two spline-interpolated autocorrelation functions from each image correlation box. The most serious contribution to peak-locking error is thus removed. The resulting velocity fields correspond, at late stages, to the horizontal velocities (u, v) at the mid-plane of the bluff body, since the vertical displacements vanish at late stages. The uncertainties in the individual velocity measurements are of the order of 1%. The vertical component of the vorticity $\omega_z = \partial v/\partial x - \partial u/\partial y$ is calculated by a smoothing spline interpolation of the velocity field with an uncertainty of less than 10%.

2.2. *Parameters of the flow*

Using the tow speed, U_B, the diameter, D, of the bluff body, the kinematic viscosity of the fluid $\nu = 1.02 \times 10^{-6}\ \mathrm{m^2\,s^{-1}}$ and the buoyancy frequency N, two non-dimensional parameters can be defined. The Reynolds number $Re \equiv U_B D/\nu$ is varied between 5000 and 33 000. It was shown in Spedding *et al.* (1996) and Spedding (1997) that the Reynolds number over this range has only a weak influence on late-time stratified wakes and its independence has not been studied in further detail here. More attention has been paid to the effect of the Froude number defined by $F \equiv 2U_B/N D$, where N is the buoyancy frequency. The Froude number is varied between 6 and 40, and for a set of experiments with fixed N, it is proportional to the Reynolds number, since D is not modified.

Meunier & Spedding (2004) demonstrated that for different shapes of bluff bodies, all the characteristics of the wake rescale when using an effective diameter (introduced as the momentum thickness by Tennekes & Lumley 1972, chapter 4) based on the drag coefficient:

$$D_{\mathrm{eff}} = D\sqrt{c_D/2}. \tag{2.1}$$

In this formula, c_D is the drag coefficient for an axisymmetric bluff body, based on the surface area $\pi D^2/4$ of the object in a plane normal to its axis. In this paper, D_{eff} is used to rescale the characteristics of the wakes with non-zero momentum. Since D_{eff} is the only relevant lengthscale in the late stages of the momentum wakes, an effective Froude number can be defined as $F_{\mathrm{eff}} = 2U_B/N D_{\mathrm{eff}}$.

The effective diameters of the bluff bodies were calculated from published measurements of the drag coefficient (Blevins 1984) in a non-stratified fluid. For the self-propelled cylinder, the drag coefficient of the cylinder alone is equal to 0.85, leading to an effective diameter $D_{\mathrm{eff}} = 0.65D$. The drag of the propeller is neglected, since it does not significantly alter the drag coefficient. The drag coefficient of a spheroid with aspect ratio 1:6 is equal to 0.176, for an effective diameter $D_{\mathrm{eff}} = 0.3D$. The drag of the propeller has again been neglected, which is a reasonable assumption when the propeller is rotating, i.e. when the towing velocity is close to the momentumless velocity. However, when the propeller is not rotating, it creates an additional drag which tends to increase D_{eff}. This willl be discussed in more detail in § 4.

2.3. *Instantaneous and mean measurements*

The non-dimensional downstream distance x/D, commonly used for non-stratified wakes in water channels and wind tunnels, is related here to the elapsed time t in the tow tank by $x/D = U_B t/D$. However, in stratified wakes, time scales with the buoyancy frequency at late stages, which defines a non-dimensional time Nt. The downstream distance is thus related to the non-dimensional time by

$$x/D = F/2\ Nt. \tag{2.2}$$

Mean quantities are obtained by averages along the streamwise direction x at a given time Nt and over the entire interrogation window length Δx. They will be denoted by $\langle\cdot\rangle_x$ and were measured on 60–80 velocity vectors. They correspond to temporal averages that would be obtained in a wind tunnel or a water channel configuration at late stages. Indeed both averages are identical when the downstream distance x is much larger than the interrogation window length Δx. This approximation is valid up to one order of magnitude for all cases here, when Nt is greater than 50.

The streamwise velocity is separated into mean and fluctuating parts,

$$(u, v) = (U, 0) + (u', v'), \tag{2.3}$$

and the following mean quantities are studied: the mean streamwise velocity $U = \langle u\rangle_x$, the quadratic fluctuations of velocity $u^* = \langle u'^2 + v'^2\rangle_x^{1/2}$ and the crossed fluctuations of velocity $\langle u'v'\rangle_x$. All of these quantities depend on the transverse coordinate y and on the non-dimensional time Nt.

3. Three regimes of the wake

Seven series of experiments were run, three with the propelled cylinder and four with the propelled spheroid. Each series was conducted in the same manner: the angular velocity of the propeller was fixed at a constant rate, the bluff body was towed with a constant velocity, and the velocity fields were estimated by CIV. From one experiment to the next, the tow speed was increased.

The patterns of the vertical vorticity fields are summarized in figure 2. The vertical component of the vorticity ω_z is shown as a function of time for three different tow speeds. The bluff bodies are always towed from right to left, i.e. in the positive x-direction.

For low tow speeds, the momentum flux expelled by the propeller is much higher than the momentum flux entrained by the bluff body due to the drag. The self-propelled body thus creates a jet of fluid toward the right (i.e. in the $-x$-direction), although the bluff body moves toward the left, as seen in figure 2(a), where the coherent structures move slowly toward the right. Since the wake is composed of two layers of opposite-signed vorticity, positive for y negative (y^-) and negative for y positive (y^+), net momentum is ejected backward by the bluff body. The jet then destabilizes into coherent vortices, which merge gradually, increasing the width of the wake.

On the contrary, for high tow speeds, there is more momentum flux created by the drag force than expelled by the propeller. Some fluid follows the bluff body and creates a leftward-moving jet. The vorticity fields look very similar to those of figure 2(a) except that the positive vorticity is found for y^+ and the negative vorticity for y^-. The wake is similar to that of a non-propelled bluff body, which is recovered when the drag force is much higher than the thrust of the propeller. In either of the two previous cases (high or low velocities), some momentum is created by the bluff

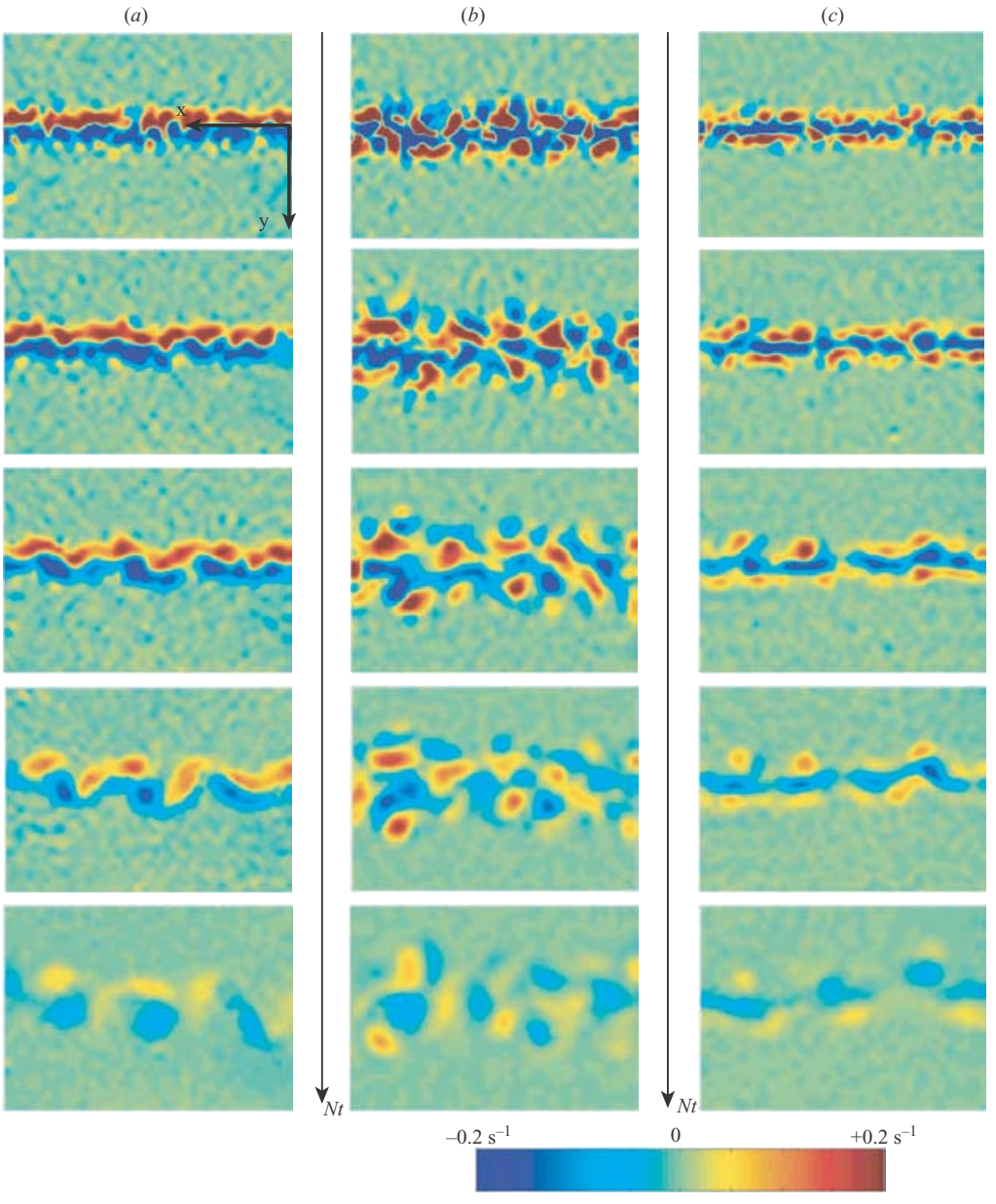

FIGURE 2. Vorticity fields of a towed body with a rotating propeller for $Nt =$ [12, 30, 60, 120, 300] from top to bottom. The bodies are towed from right to left at a speed (*a*) lower than the momentumless velocity, (*b*) equal to the mometumless velocity, and (*c*) equal to the momentumless velocity with an angle of attack. The bluff body is a prolate spheroid for (*a*) and (*c*) and a cylinder for (*b*). The field of view has dimensions $80 \times 60\,\mathrm{cm}^2$, corresponding to 32×23 diameters. $F \approx 20$; $Re \approx 15\,000$.

body and the treatment of the data is essentially the same, as described in detail in § 4, which focuses on this momentum regime.

Between the two previous cases with a backward jet at small U_B and a forward jet at high U_B, there is a limiting case where the jet eventually vanishes. It happens for

a particular (critical) value of the tow speed $U_B = U_C$, where no net momentum is created. Intuitively, its value is proportional to the angular velocity of the propeller. U_C is thus a way of measuring the angular velocity of the propeller, and to recalibrate it with no need to take into account the shape of the propeller and the bluff body. In the experiments, this critical momentumless velocity is defined by the criterion that the sum of the mean profile vanishes:

$$U_B = U_C \quad \text{when} \quad \int_{-\infty}^{\infty} \langle u \rangle_x \, \mathrm{d}y = 0. \tag{3.1}$$

This criterion defines U_C to within $\pm 2\%$, and if U_B is changed by more than 2%, the late stages of the wake resemble one of the cases mentioned above (high or low U_B). Only by careful matching of U_B to U_C was it possible to reach the momentumless regime, for which the mean profile of velocity vanishes in the incoherent fluctuations of the measurements. An example is shown in figure 2(*b*). The two layers of vorticity found in the momentum regime have disappeared and the vorticity field contains many vortices of both signs, with no organized longitudinal spatial structure. Like-signed vortices merge, leading to larger scales of motion, whose peak vorticity magnitude decreases gradually with time. This momentumless regime will be described in detail in § 5.

Finally, a third regime has been found incidentally. In the first experiments, a slight angle of attack was present between the axis of the bluff body and the towing direction. The angle of attack (measured between the guide cable and the axis of the propeller) was smaller than 1° and had no influence on the momentum regime. However, when the tow speed was close to the momentumless velocity U_C, the wake became asymmetric. Since the bluff body was oriented slightly toward y^+, the fluid expelled by the propeller was slightly to y^-. This leads to three layers of vorticity: two layers of positive vorticity surround a layer of negative vorticity, as can be observed in figure 2(*c*). This regime is very similar to the momentum regime except that there are three layers of vorticity instead of two. These three layers destabilize into vortices, as in the momentum regime, which merge into bigger vortices, thus increasing the wake width. This regime will be described in detail in § 6.

4. Momentum regime

4.1. *Mean profiles*

In the momentum regime (figure 2*a*), the mean velocity is larger than the fluctuations. Figure 3 shows the transverse profile of mean velocity $U(y) = \langle u \rangle_x(y)$ as filled symbols, together with the profile of the quadratic fluctuations of velocity $u^* = \langle u'^2 + v'^2 \rangle_x^{1/2}$ as open symbols. It is clear that the fluctuations are smaller than the mean velocity up to $Nt = 300$.

Figure 3 shows that the mean profiles of velocity can be fitted well by a Gaussian function (shown as a solid line on figure 3) with amplitude U_0 and half-width L_0,

$$U(y) = U_0 \, \mathrm{e}^{-y^2/2L_0^2}. \tag{4.1}$$

As time increases, the amplitude U_0 decreases and the wake width L_0 increases, as is found in both stratified and non-stratified wakes of non-propelled bodies.

In the case of propelled bodies, the amplitude U_0 of the wake can be either positive or negative, depending on whether the towing velocity U_B is larger or smaller than the critical velocity U_C. Indeed, when U_C is smaller than U_B, i.e. when the propeller rotates slowly, the bluff body is similar to a non-propelled body and the amplitude

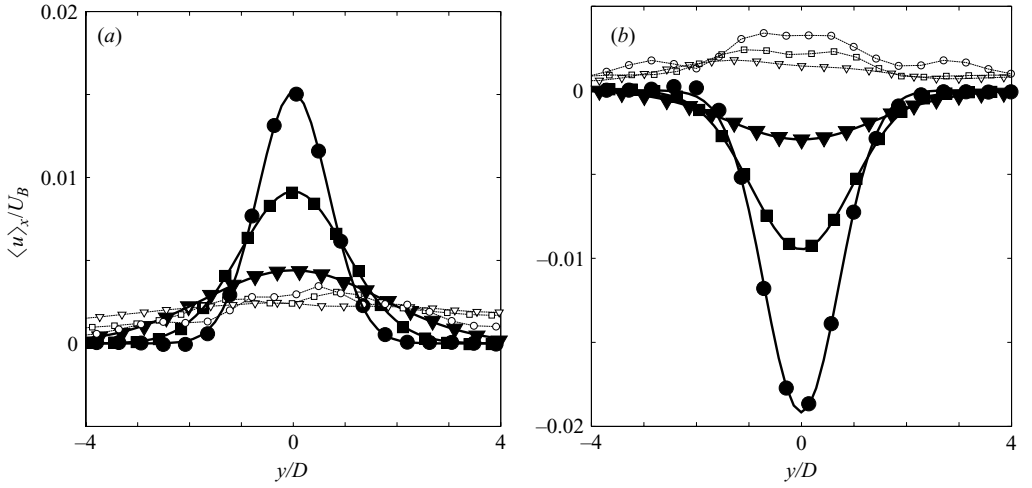

FIGURE 3. Profile of mean velocity (filled symbols) and quadratic fluctuations $\langle u'^2 + v'^2 \rangle_x^{1/2}$ (open symbols) at times $Nt = 20$ (●), $Nt = 100$ (■) and $Nt = 300$ (▼). The spheroid is towed at (*a*) a speed larger than the momentumless velocity ($U_B = 1.13U_C$) and (*b*) a speed smaller than the momentumless velocity ($U_B = 0.88U_C$). The Froude and the Reynolds numbers are: (*a*) $F = 14$, $Re = 11\,000$; (*b*) $F = 18$, $Re = 9000$.

of the wake U_0 is positive. This means that some fluid is entrained behind the body by the drag. On the other hand, when U_C is larger than U_B, i.e. when the body is towed slowly, some fluid is expelled backwards by the propeller, creating a jet in the $-x$-direction, which gives a negative amplitude U_0.

As U_C/U_B is increased (obtained in the experiments by decreasing U_B and keeping U_C constant), the amplitude of the wake decreases continuously from positive to negative values. This is shown in figure 4 where $U_0/U_B\ F_{\text{eff}}^{2/3}$ is plotted as a function of the ratio U_C/U_B for $Nt = 100$. All the results collapse well in these units. The curve has a steep gradient at $U_C = U_B$ so even a very small variation in U_B can create a large amplitude U_0 in the wake. This explains why it was very hard in the experiment to obtain a momentumless regime, and why most of the experiments were found to be in the momentum regime. When the tow speed U_B differs from the momentumless velocity U_C by more than 2%, the amplitude of the wake U_0 cannot be neglected and the wake is in the momentum regime.

4.2. *A new definition of the momentum thickness for propelled bluff bodies*

The absolute amplitude of a stratified wake depends strongly on the shape of the bluff body (see Meunier & Spedding 2004). However, the results were found to collapse when using an effective diameter based on the drag coefficient and defined by equation (2.1), leading to a universal law for non-propelled bodies:

$$\frac{U_0}{U_B} F_{\text{eff}}^{2/3} = 6.6(Nt)^{-0.76}, \tag{4.2}$$

where $F_{\text{eff}} = 2U_B/ND_{\text{eff}}$. In the case of propelled bodies, this law is expected to apply only when the propeller is not rotating, i.e. when $U_C = 0$, shown as a star in figure 4. It is 30% smaller than the experimental value for a spheroid, which can be explained quantitatively by the additional drag created by the non-rotating propeller.

The evolution of $U_0(Nt)$ is shown in figure 5(*a*) for varying tow speeds U_B. The dashed line shows the empirical curve for non-propelled bodies given by equation (4.2).

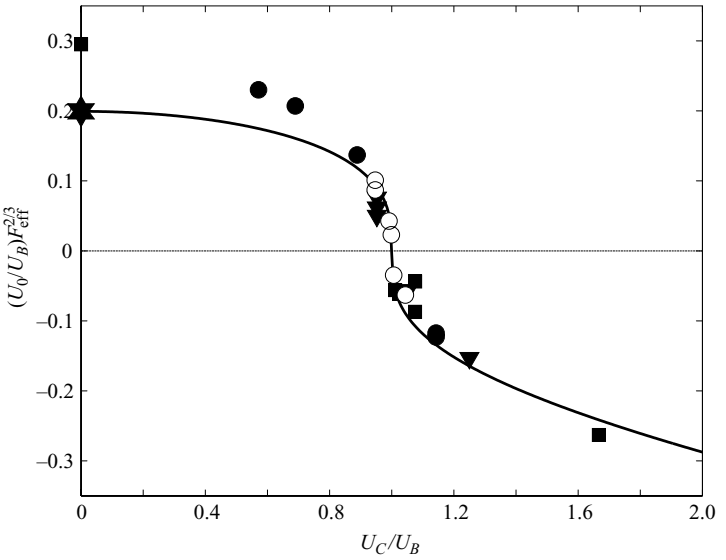

FIGURE 4. Amplitude of the mean profile of velocity as a function of the velocity of the propeller for a spheroid (closed symbols) and a cylinder (open symbols) at $Nt = 100$. The solid star represents the prediction given by Meunier & Spedding (2004) for non-propelled bodies. The solid line is from equation (4.5), developed in § 4.2.

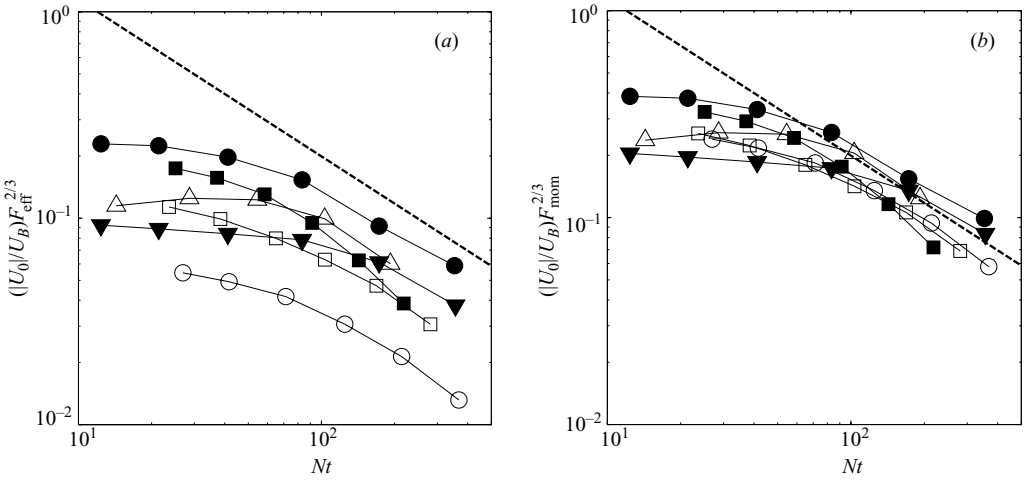

FIGURE 5. Amplitude of the mean profile of velocity for a cylinder (open symbols) and for a spheroid (closed symbols) using (*a*) the effective diameter defined by (2.1) and (*b*) the momentum thickness defined by (4.3). The ratios of U_B/U_C of towed and momentumless velocity are [0.994, 0.959, 1.063, 1.125, 0.930, 1.050] for [○, □, △, ●, ■, ▼]. $F = [15, 14, 27, 18, 23, 41]$ and $Re = [10.5, 10.1, 28.4, 11.4, 15.2, 26.6] \times 10^3$ respectively.

In all these experiments, the scaling exponent seems to be equal at late stages, but the curves always remain below the non-propelled case. The model must therefore be modified to take into account the action of the propeller.

In the case of non-propelled bodies, the dynamics of the wake are mainly governed by the momentum flux, which is a conserved quantity of the wake. Indeed, the effective

diameter $D_{\rm eff}$ is simply the momentum thickness, already introduced in non-stratified wakes by (Tennekes & Lumley 1972, chapter 4), and which is found by equating the momentum flux $J = \rho \frac{1}{4}\pi D_{\rm eff}^2 U_B^2$ and the drag force $F_{\rm drag} = c_D \frac{1}{2}\rho U_B^2 \frac{1}{4}\pi D^2$.

For propelled bodies, the momentum comes from fluid entrained by the drag, and also from fluid expelled by the propeller, which creates the thrust: $J = F_{\rm drag} - F_{\rm thrust}$. By definition of the momentumless velocity U_C, the thrust is equal to the drag for $U_B = U_C$, which leads to an expression for the thrust: $F_{\rm thrust} = c_D \frac{1}{2}\rho U_C^2 \frac{1}{4}\pi D^2$. A momentum thickness can thus be defined in the case of propelled bodies as $\rho \frac{1}{4}\pi D_{\rm mom}^2 U_B^2 = |J| = |F_{\rm drag} - F_{\rm thrust}|$, which can be simplified into

$$D_{\rm mom} = D\sqrt{c_D/2}\sqrt{|1 - U_C^2/U_B^2|}. \tag{4.3}$$

The universal law (4.2) found for non-propelled bodies should be modified to

$$\frac{|U_0|}{U_B} F_{\rm mom}^{2/3} = 6.6(Nt)^{-0.76}, \tag{4.4}$$

where the momentum Froude number is defined using the momentum thickness, $F_{\rm mom} = 2U_B/N D_{\rm mom}$. Equation (4.4) is plotted in figure 5(*b*) as a dashed line. All the results collapse onto this prediction to within 25%, even though they were initially as much as 6 times smaller. Furthermore, if the momentum Froude number in equation (4.4) is explicitly written with (4.3) one arrives at an expression for the amplitude U_0 as a function of the ratio U_C/U_B,

$$\frac{|U_0|}{U_B} F_{\rm eff}^{2/3} = 6.6(Nt)^{-0.76}|1 - (U_C/U_B)^2|^{1/3}. \tag{4.5}$$

This curve is plotted in figure 4 as a solid line. The vertical slope at $U_C = U_B$, observed in the experimental data, comes from the power 1/3 of the term $U_B - U_C$ in (4.5), and the dependence on $|U_B - U_C|^{1/3}$ explains the overall features of the curve.

4.3. *Wake width and Strouhal number*

The wake width L_0 of the mean profile of velocity, defined by equation (4.1), is plotted in figure 6 as a function of time. The wake width increases in time with a power law close to 0.3. For non-propelled bodies, it was shown in Meunier & Spedding (2004) that the wake width of different bluff bodies collapses when the lengthscale is defined as the effective diameter $D_{\rm eff}$, and can be written as

$$\frac{L_0}{D_{\rm eff}} F_{\rm eff}^{-0.35} = 0.275(Nt)^{0.35}. \tag{4.6}$$

This prediction is plotted in figure 6(*a*) as a dashed line. The experimental values obtained for propelled bodies are smaller than the theoretical prediction for non-propelled bodies, by a factor almost two. Recall that the wake is slower for propelled bodies, with a smaller amplitude U_0, and the wake width thus increases more slowly at early stages and remains smaller than for a non-propelled body.

To adapt the prediction made for non-propelled bodies to the case of propelled bodies, the wake width can be normalized by the momentum thickness $D_{\rm mom}$ defined in (4.3), rather than by the effective diameter $D_{\rm eff}$. If the Froude number is also defined using the momentum thickness $D_{\rm mom}$, (4.6) is modified to

$$\frac{L_0}{D_{\rm mom}} F_{\rm mom}^{-0.35} = 0.275(Nt)^{0.35}. \tag{4.7}$$

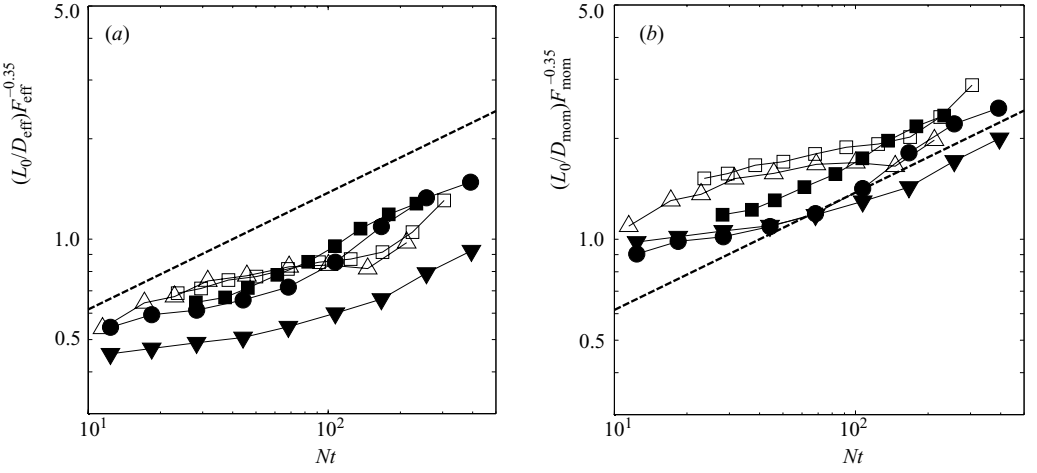

FIGURE 6. Wake half-width of the mean profile of velocity for a cylinder (open symbols) and for a spheroid (closed symbols) using (*a*) the effective diameter and (*b*) the momentum thickness. Symbols as in figure 5.

The modified prediction is shown in figure 6(*b*) by the dashed line. The experimental data collapse reasonably well onto this power law at late stages. The measurements are centred on the dashed line, although the variation in the measurements is relatively high (close to 30%). The scatter is due to the small amplitude of the wake U_0 compared to the towing velocity U_B of the bluff body: U_0/U_B can be as small as 0.1%. It is surprising to see that the simple rescaling using the momentum thickness $D_{\rm mom}$ is also efficient for the wake width, as it was for the velocity defect. It confirms the fact that the late stages are mainly governed by the momentum, without memory of the lengthscale of the bluff body. However, in the early stages, the wake width is slightly higher than the value given by the prediction (4.7). This might be due to a transient effect: when the towing velocity is close to the momentumless velocity, the wake motions are very slow and it takes a longer time (which could be rescaled by $D/(U_B - U_C)$ rather than D/U_B) for the wake to reach the asymptotic self-preserved state.

The Strouhal number can be measured from the instantaneous vorticity fields, as explained in Spedding *et al.* (1996) and Spedding (2002) for the stratified wake of a sphere. The Strouhal number can be defined as

$$St = D/\lambda_x, \tag{4.8}$$

where λ_x is the mean streamwise distance between two vortices of the same sign. It was shown in Meunier & Spedding (2004) that a general law for the Strouhal number can be found in the case of non-propelled bodies by defining the Strouhal number using the effective diameter,

$$St_{\rm eff} = D_{\rm eff}/\lambda_x. \tag{4.9}$$

With this definition all the measurements of different bluff bodies collapsed onto a universal law,

$$St_{\rm eff} F_{\rm eff}^{0.34} = 0.823(Nt)^{-0.34}, \tag{4.10}$$

plotted in figure 7(*a*) as a dashed line. The experimental values are twice as large, but decay at the same rate. Recall that propelled wakes develop more slowly than

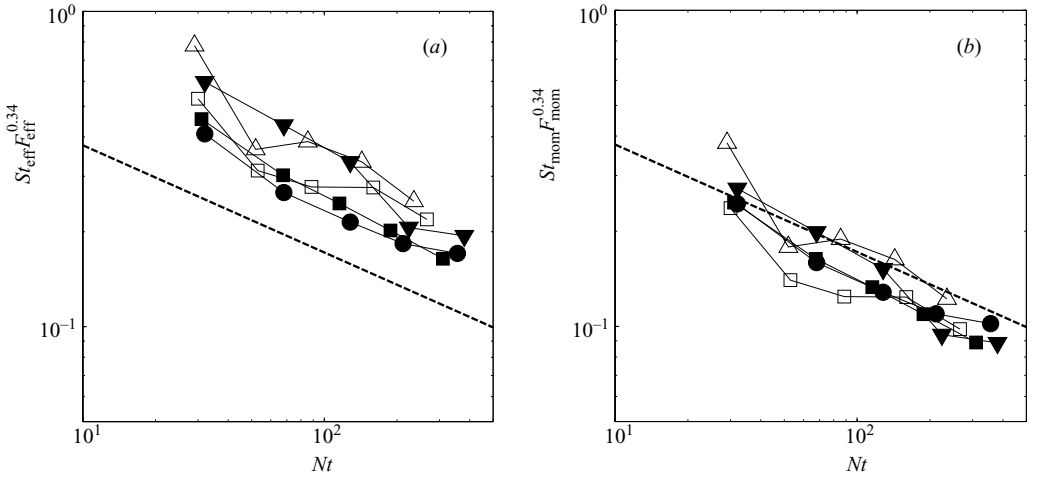

FIGURE 7. Strouhal number based on the distance between two vortices of the same sign for a cylinder (open symbols) and for a spheroid (closed symbols) using (*a*) the effective diameter and (*b*) the momentum thickness. Symbols as in figure 5.

non-propelled wakes (since U_0 is smaller), so the Strouhal number also decreases more slowly at early stages, and stays larger than for non-propelled bodies.

If the Strouhal number is defined using the momentum thickness $D_{\rm mom}$ defined in (4.3), and if the Froude number is also defined using the momentum thickness $D_{\rm mom}$, the prediction for non-propelled bodies is

$$St_{\rm mom}F_{\rm mom}^{0.34} = 0.823(Nt)^{-0.34}, \tag{4.11}$$

and is plotted as a dashed line in figure 7(*b*). The experimental data collapse onto the prediction, within 20%. This shows again that the wake is governed by the momentum flux at late stages.

4.4. *Fluctuating quantities*

In self-preserved, turbulent wakes, the mean profile of the wake diffuses due to the Reynolds stress, which is sustained by the mean shear. The hypothesis of a constant eddy viscosity can be checked for the case of stratified and propelled wakes, and if ν_T is constant, the profile of Reynolds stress may be supposed to be proportional to the mean shear,

$$\langle u'v'\rangle_x = \nu_T \frac{\partial U}{\partial y}. \tag{4.12}$$

Profiles of Reynolds stress, or velocity cross-fluctuations, are shown in figure 8 for tow speeds, U_B, close to the critical momentumless velocity, U_C. The Reynolds stress are very weak and $\langle u'v'\rangle^{1/2}$ is always smaller than 0.1% of U_B. When $U_B > U_C$, the mean profile has a positive amplitude U_0; the mean shear is thus positive for y^- and negative for y^+. Figure 8(*a*) shows that the cross-fluctuations follow the same trend for $U_B > U_C$, supporting the assumption that the profile of Reynolds stress is proportional to the mean shear, with a constant eddy viscosity. When the bluff body is towed at a velocity smaller than the momentumless velocity, the amplitude of the wake U_0 is negative, which gives negative Reynolds stress for y^- and positive Reynolds stress for y^+, as shown on figure 8(*b*), again proportional to the mean shear.

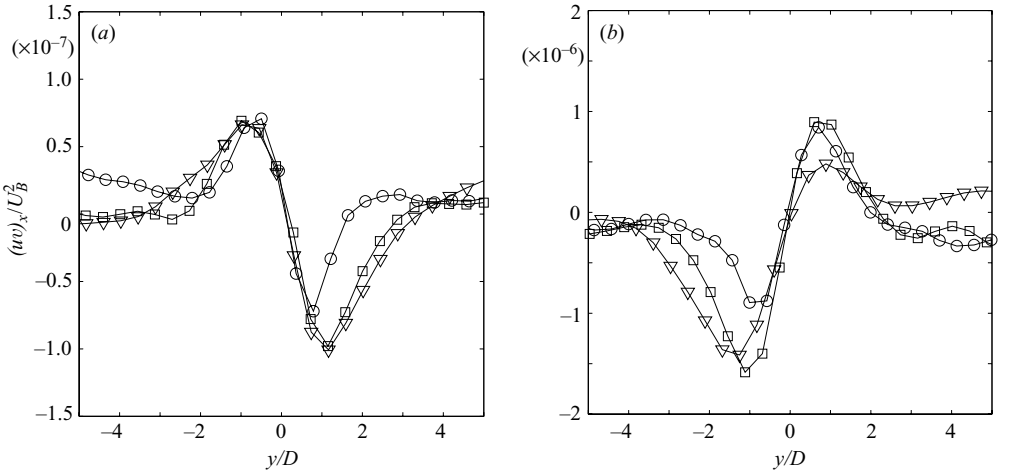

FIGURE 8. Profile of cross-fluctuation velocity $\langle u'v' \rangle_x$ at times $Nt = 60$ (○), $Nt = 120$ (□) and $Nt = 240$ (▽). The spheroid is towed at speed (*a*) larger than the momentumless velocity ($U_B = 1.05U_C$) and (*b*) smaller than the momentumless velocity ($U_B = 0.88U_C$). The Froude and the Reynolds numbers are: (*a*) $F = 41$, $Re = 26,000$; (*b*) $F = 14$, $Re = 9000$.

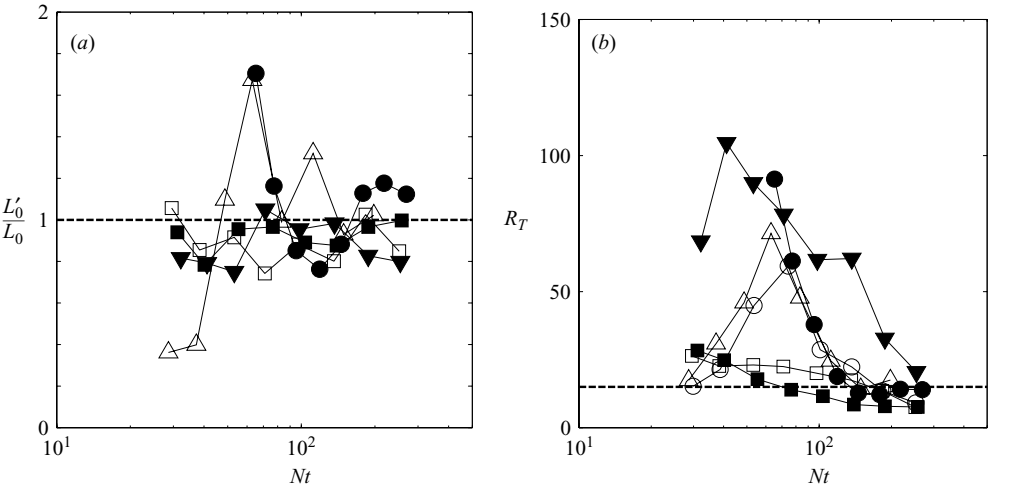

FIGURE 9. (*a*) Wake width of the profile of cross-fluctuations, and (*b*) turbulent Reynolds number, defined by (4.13) and (4.14). Symbols as in figure 5.

Since the mean profile of velocity is approximated well by a Gaussian (4.1) with amplitude U_0, the Reynolds stress profile should be fitted well by the derivative of a Gaussian function with an amplitude A and a width L_0':

$$\langle u'v' \rangle_x(y) = -A \frac{y}{L_0'} \mathrm{e}^{-y^2/L_0'^2}. \tag{4.13}$$

The amplitude A should be similar to $\nu_T U_0$ and the width L_0' should be similar to the wake width L_0. These two fitting constants have been measured and are shown in figure 9. The width of the cross-fluctuation profile L_0' is close to the wake width L_0 (figure 9*a*) although the variation in the measurements is large. This supports once again the hypothesis of a constant eddy viscosity. The amplitude A of the

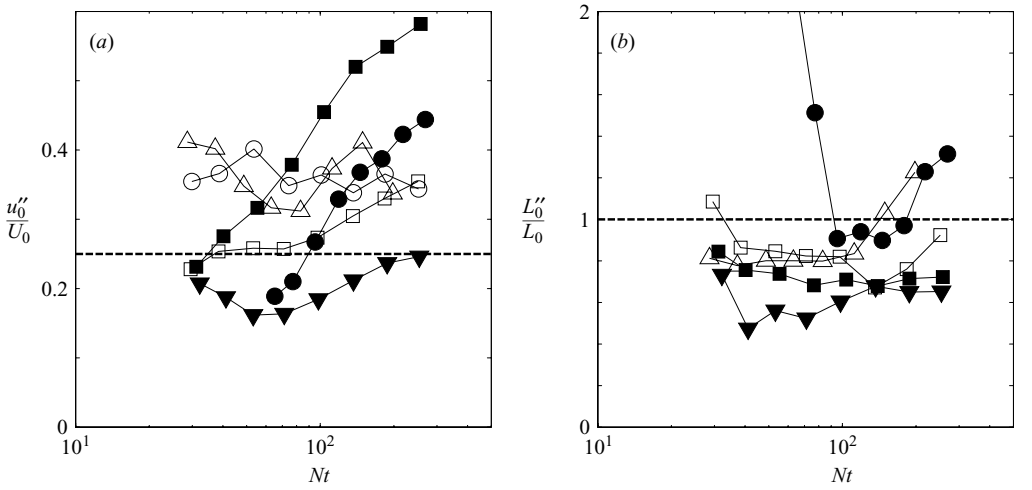

FIGURE 10. (*a*) Amplitude and (*b*) half-width of the profile of the quadratic fluctuations. Symbols as in figure 5.

cross-fluctuation profile is linked to the turbulent Reynolds number R_T by

$$R_T = \frac{|U_0|L_0}{\nu_T} = \frac{U_0|U_0|}{A}. \tag{4.14}$$

The turbulent Reynolds number is plotted in figure 9(*b*) as a function of time. The dashed line represents the value $R_T = 15$ found for non-propelled bodies at late times ($Nt > 100$). Initially, R_T can be significantly higher than its asymptotic value for $Nt > 100$, which is the same result as for towed bodies, suggesting that, just as in the non-propelled case for these body shapes, an equilibrium state is only reached at comparatively late times.

For a complete analysis of the turbulent fluctuations, the turbulent kinetic energy, equal to half the quadratic fluctuations of velocity $u^* = \langle u'^2 + v'^2 \rangle^{1/2}$ is measured. A profile of quadratic fluctuations of velocity was shown in figure 3, and seen to be very small compared to the mean profile. Moreover, the presence of large internal waves in the tank creates a background of velocity variations, which are of the order of the velocity fluctuations created by the wake. This background can be seen on figure 3 at the edges of the profile. The amplitude of the quadratic fluctuations was estimated by measuring the difference between the maximum and the minimum of the profile of quadratic fluctuations,

$$u_0'' = \max\left(\langle u'^2 + v'^2 \rangle^{1/2}\right) - \min\left(\langle u'^2 + v'^2 \rangle^{1/2}\right). \tag{4.15}$$

This amplitude is plotted in figure 10(*a*) as a function of time. The measurements are not very clean, but the ratio u_0''/U_0 is close to the value 0.25, which was found for non-propelled bodies and which is shown as a dashed line on figure 10(*a*).

Finally, the width of the profile of quadratic fluctuations was estimated by a fitting function introduced by Dommermuth *et al.* (2002):

$$\langle u'^2 + v'^2 \rangle^{1/2} = B + C\left(1 + y^2/L_0''^2\right)\mathrm{e}^{-y^2/2L_0''^2}. \tag{4.16}$$

L_0'' is normalized by the wake width L_0 and plotted in figure 10(*b*). The ratio L_0''/L_0 is slightly smaller than one, as in the case of non-propelled bodies. This may be due to transient effects, since the self-preserved state is only reached for very late stages.

5. Momentumless regime

As demonstrated in § 3, the wake presents a different structure when the towing velocity U_B of the bluff body is equal to the momentumless velocity U_C. The vorticity fields do not contain two layers of opposite-sign vorticity, as in the momentum regime ($U_B \neq U_C$), but they contain a disordered array of vortices of different signs. There seems to be no organized structure, except that the vortices are located in a compact domain that trails the body and widens with time.

The momentumless regime is only accessible when the relative difference between U_B and U_C is smaller than 2%. The primary difficulty in the experiments was in determining U_C, which was done by iteration for each angular velocity of the propeller, so that for each experiment, the mean velocity profile was measured and the towing velocity was then adjusted for the next experiment. Since at least 20 minutes waiting time (frequently many times this, depending on flow conditions) was required between two experiments for the fluid to be effectively at rest, a long time (usually a few days) was needed to determine the exact momentumless velocity for a given angular velocity of the propeller. Although this momentumless regime might represent the wakes of self-propelled bodies, it was evidently very hard to obtain in the experiments, and was very fragile compared with the momentum regime. The question of whether the wake of a real self-propelled body is in the momentum or in the momentumless regime will be discussed in § 7.

When $|U_B - U_C|/U_B < 2\%$ the signal:noise ratio is (by definition) small, and particular care was taken to repeat each experiment several times, and to remove all spurious results caused by contamination from wave motions or imperfect boundary conditions. All points shown are averages of the remaining two to four clean experiments.

5.1. *A null mean profile?*

When $U_B > U_C$, U_0 is positive and when $U_B < U_C$, U_0 is negative, so U_0 might be expected to vanish when $U_B = U_C$. However, in the constant turbulent eddy viscosity assumption of Tennekes & Lumley (1972), it is only the integral of the mean profile that vanishes, and not the mean profile itself. The mean profile is supposed to contain a central lobe with negative velocity, surrounded by two symmetric lobes of positive velocity. This shape of the mean velocity profile ensures that the turbulent fluctuations are still sustained by the mean shear. More sophisticated treatments (Finson 1975; Hassid 1980) invoke assumptions on higher-order closure of the fluctuating velocities, but some coherent form of the mean radial profile of the velocity differences is still required. Some kind of assumption like this is a necessary condition in order to impose self-similar solutions.

The measured mean velocity profiles are plotted in figure 11 as closed symbols, for the wake of a cylinder and the wake of a spheroid. The mean profile has no coherent shape, and seems to be smaller than the incoherent fluctuations in the measurements. It does not contain the features described in non-stratified wakes, with a positive lobe surrounded by two negative lobes. It is possible that such a structure of the wake could be recovered if the measurement resolution were higher (or, equivalently, at smaller x/D), or if the generating geometry were different. However, figure 11 shows that the quadratic fluctuations of velocity are larger than the mean velocity: they can be as much as five times larger in the case of the cylinder. This contradicts the assumption that the turbulent fluctuations are sustained by the mean shear. This regime is best described as a turbulent flow, with no mean shear, which diffuses and dissipates by self-induction. Such a description of the wake is consistent (of course)

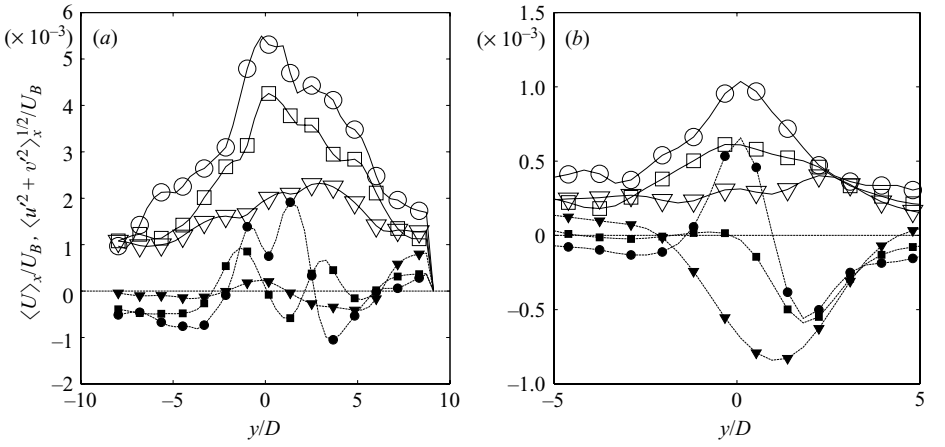

FIGURE 11. Profile of mean velocity (filled symbols) and quadratic fluctuations (open symbols) at times $Nt = 50$ (○), $Nt = 100$ (□) and $Nt = 300$ (▽) for (*a*) a cylinder with $F = 25$ and $Re = 27\,000$, (*b*) a spheroid with $F = 40$ and $Re = 25\,000$.

with the vorticity fields of figure 2(*b*), where no organized structure can be found. Now, the evolution of the wake should be governed by the fluctuations of the velocity rather than by the mean velocity of the wake.

5.2. *Quadratic fluctuations*

The profile of quadratic fluctuations of velocity $u^* = \langle u'^2 + v'^2\rangle^{1/2}$ is plotted in figure 11 as open symbols, for a cylinder and for a spheroid. The quadratic fluctuations are very small: between 0.1% and 0.5% of the towing velocity U_B. Moreover, the bluff body creates internal waves of large amplitude, propagating in the x-direction, which remain in the tank for a long time due to reflection on the walls. Their amplitude can be measured by the average of the streamwise velocity in the y-direction $\langle u\rangle_y(x)$ and they were removed from the velocity field before measuring the quadratic fluctuations of velocity. However, these internal waves also created some small-scale variations which cannot be averaged out in this way, especially far from the wake (for large $|y|$), which leads to a positive background in the profiles of quadratic velocity fluctuations. Consequently the width of the wake cannot be measured accurately using the profile of velocity fluctuations. It will be instead measured using the profile of vorticity flucuations (see § 5.3), which are not perturbed by the internal waves since the internal waves do not contain any vertical vorticity.

The maximum of the profile of velocity fluctuations can be relatively accurately measured. It is plotted in figure 12 for the five different configurations studied for this momentumless regime. Each curve is the average of two to four experiments. The variation in the measurements is represented by the size of the symbols.

The maximum of the quadratic fluctuations $u^*_{\max} = \max(\langle u'^2 + v'^2\rangle^{1/2})$ is plotted as $u^*_{\max}/U_B F^{0.75}$ so the results may be compared with the measurements obtained by Lin & Pao (1979) for a streamlined spheroid, plotted as a solid line on this figure. The current measurements are significantly smaller, the velocity being four times smaller at early stages. Moreover, assuming the quadratic velocity has a power law $u^*_{\max} \sim (Nt)^{\alpha_{u^*}}$, Lin & Pao measured a decay exponent of -0.76, whereas we find

$$\alpha_{u^*} = -0.40 \pm 0.04. \tag{5.1}$$

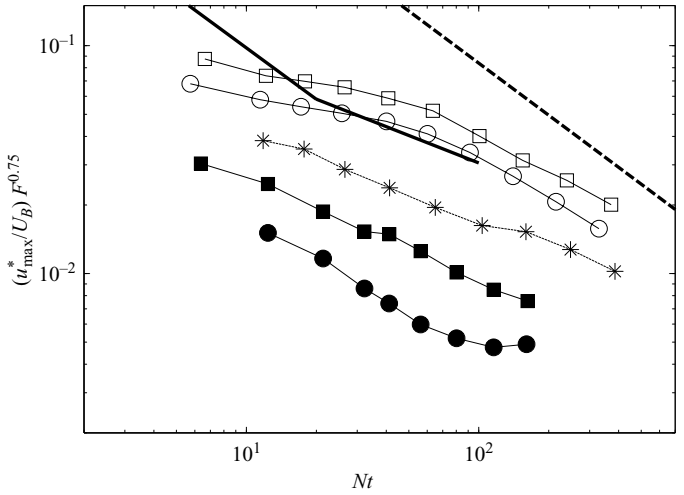

FIGURE 12. Amplitude of the quadratic fluctuations of velocity $u^* = \langle u'^2 + v'^2 \rangle_x^{1/2}$ for a slender spheroid (closed symbols), a cylinder with a small propeller (open symbols) and a cylinder with a large propeller (*). The solid line corresponds to the experimental fit given by Lin & Pao (1979), and the dashed line corresponds to the amplitude of the mean velocity of a towed slender body given by Meunier and Spedding (2004). $F = [15, 40, 12, 15, 25]$ for experiments [●, ■, *, ○, □] with $Re = [10, 25, 11, 13, 27] \times 10^3$ respectively.

The disagreement comes partly from the fact that the results of Lin & Pao (1979) were restricted to the early stages of the wake: their scaling is valid for $1 < Nt < 20$ while our results cover $10 < Nt < 300$. At the early stages, the flow is mainly three-dimensional, which might explain why they measure a decay exponent $\alpha_{u^*} = -0.76$, more in agreement with the theoretical prediction for a non-stratified self-propelled wake ($\alpha_u = -4/5$). Upon close inspection, their measurements even show that the quadratic fluctuations of velocity depart from the initial power law for $Nt > 20$, as the authors noted. A decay exponent for this latter regime can be roughly estimated to be $\alpha_u = -0.4$ for $20 < Nt < 60$, in close agreement with our value for $10 < Nt < 300$.

In figure 12, two experiments with the same bluff body (a cylinder) and with two different sizes of propeller have been reported: the case of a large propeller is plotted by stars and the case of a small propeller is plotted by open symbols. The velocity fluctuations are 60% higher in the case of a small propeller. Evidently the results cannot be collapsed by simply using the drag coefficient of the bluff body alone. The amplitude of the quadratic fluctuations depends on the shape of the bluff body and the propeller, and not only on the drag coefficient of the bluff body (here, the drag of the propeller is small compared to the drag of the cylinder). It is possible that the fluctuations depend on the shape of the bluff body close to the propeller, since the propeller draws the fluid inward and deforms the set of streamlines that would be created in the absence of a propeller. The small propeller may draw the fluid into a smaller cross-section, forcing streamlines closer to the edges of the cylinder, and so creating strong turbulence.

It can be noted that the measurements do not collapse with respect to the Froude number when the velocity fluctuation is multiplied by $F^{0.75}$. A better collapse of the measurements is obtained when the velocity fluctuation is multiplied by $F^{0.25}$. However, the Froude number was varied with a factor 3 only, and the measurements should be repeated on a larger range of Froude numbers for this result to be confirmed.

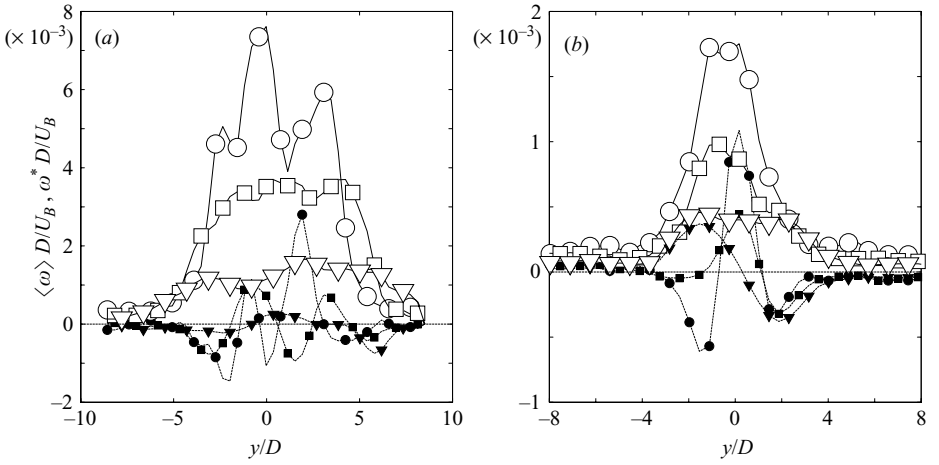

FIGURE 13. Profile of mean vorticity (filled symbols) and quadratic fluctuations of vorticity $\omega^* = \sqrt{\langle\omega^2\rangle_x}$ (open symbols) at times $Nt = 50$ (○), $Nt = 100$ (□) and $Nt = 300$ (▽) for (*a*) a cylinder with $F = 25$ and $Re = 27\,000$, (*b*) a spheroid with $F = 40$ and $Re = 25\,000$.

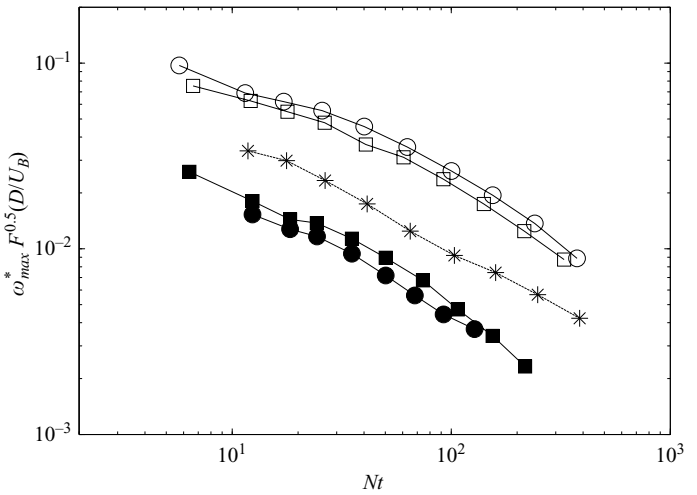

FIGURE 14. Amplitude of the maximum quadratic fluctuations of vorticity $\omega^* = \langle\omega^2\rangle_x^{1/2}$ for a slender spheroid (closed symbols), a cylinder with a small propeller (open symbols) and a cylinder with a large propeller (∗). Symbols as in figure 12.

5.3. *Vorticity fluctuations*

As noted in § 5.2, the vorticity profiles are not disturbed by internal waves which do not contain any vertical vorticity. The profiles of mean vorticity $\langle\omega\rangle$ and of the quadratic fluctations of vorticity $\omega^* = \sqrt{\langle\omega^2\rangle_x}$ are therefore less variable than the profiles of velocity. They are plotted in figure 13 for a cylinder and a spheroid. The mean vorticity is very small compared with the fluctuations. This shows again that the wake seems to be disordered, closer to a layer of free turbulence rather than to turbulence forced by the mean shear.

The maximum of the quadratic fluctuations of vorticity $\omega^*_{\max}$ is plotted in figure 14 as a function of time for a cylinder and for a spheroid. As previously noted, it is not possible to rescale the experiments by simply using the effective diameter of the bluff

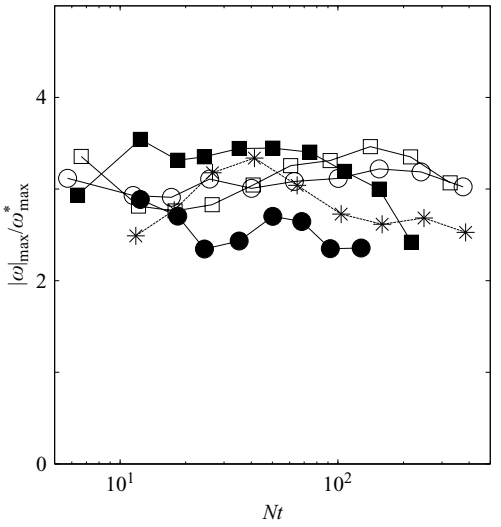

FIGURE 15. Maximum of the vorticity magnitude $|\omega|$ for a slender spheroid (closed symbols), a cylinder with a small propeller (open symbols) and a cylinder with a large propeller (*). Symbols as in figure 12.

body, since the size of the propeller strongly modifies the amplitude of the vorticity fluctuations. However, a reasonable collapse of the measurements has been obtained by multiplying the amplitude by the Froude number to the power 0.5. This empirical scaling (which has no external justification) needs to be verified since the Froude number was only varied with of a factor 3. Assuming the vorticity fluctuations follow a power law Nt^{α_ω}, the decay exponent α_ω can be estimated as

$$\alpha_\omega = -0.61 \pm 0.02. \tag{5.2}$$

Finally, the maximum of the absolute value of the vorticity $|\omega|_{\max}$ on the centreplane has been measured and is plotted as a function of time in figure 15; $|\omega|_{\max}$ is constant and roughly equal to three times the maximum of the quadratic fluctuations of vorticity, $\omega^*_{\max}$. This implies that some aspect of the spatial structure of the wake is constant, and that the wake may be self-similar in this measure.

5.4. *Wake width*

Since the profiles of quadratic fluctuations are relatively clean, it is possible to measure the width L_ω of the profile at mid-height, defined as the range for which the quadratic vorticity is larger than half the maximum quadratic vorticity:

$$\omega^*(y) > \frac{\omega^*_{\max}}{2} \text{ for } -\frac{L_\omega}{2} < y < \frac{L_\omega}{2}. \tag{5.3}$$

The width L_ω is plotted in figure 16 for five different set of experiments. In figure 16(*a*), the width is normalized using the effective diameter of the bluff body, as in the case of a momentum wake (see § 4.3). It seems that the experiments for a cylinder with a large (stars) and with a small propeller (open symbols) give the same result. This indicates that the wake width may be independent of the real shape of the bluff body and that it may be collapsed using the drag coefficient. Indeed, when plotting the wake width multiplied by the drag coefficient to the power −0.8, an excellent collapse is obtained for the case of both a spheroid and a cylinder, as is shown in figure 16(*b*).

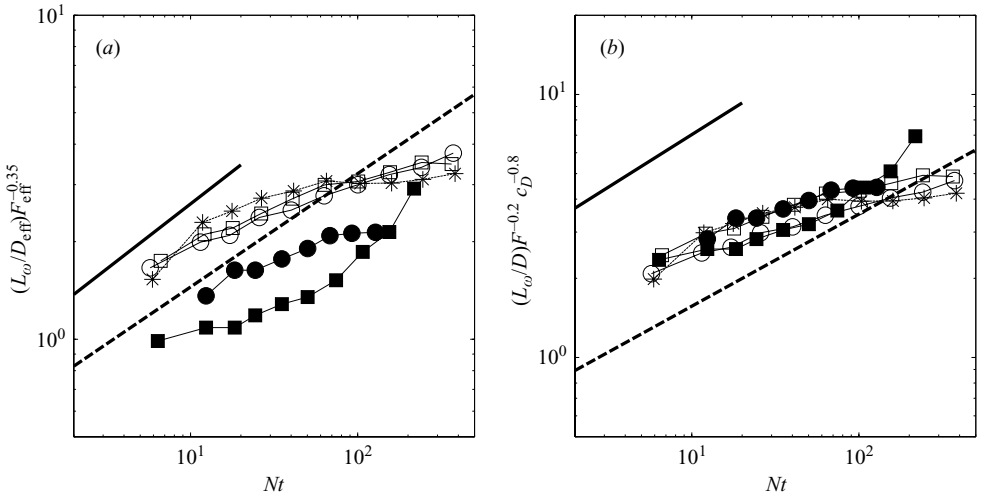

FIGURE 16. Width L_ω of the quadratic fluctuations of vorticity $\omega^* = \langle\omega^2\rangle_x^{1/2}$ for a slender spheroid (closed symbols), a cylinder with a small propeller (open symbols) and a cylinder with a large propeller (*), (*a*) normalized using the effective diameter and (*b*) multiplied by $c_0^{-0.8}$. The solid line corresponds to the experiments of Lin & Pao (1979) obtained through visualizations, and the dashed line corresponds to the mean velocity profile of a towed body (Meunier & Spedding 2004). Symbols as in figure 12.

The best fit for all the data is given by

$$\frac{L_\omega}{D} = 1.8(Nt)^{0.18} F^{0.2} c_D^{0.8}. \tag{5.4}$$

This wake width is three times smaller than the one measured by Lin & Pao (1979), plotted as a solid line on figure 16. However, this is not a real disagreement since they measured the width for which the wake appeared turbulent on the corresponding shadowgraph visualizations, which will be larger than the width at mid-height. The main disagreement comes from the fact that the exponent for their power law is equal to +0.4 whereas here it is

$$\alpha_{L_\omega} = +0.18 \pm 0.05. \tag{5.5}$$

Part of the discrepancy may again come from the fact that their measurements were obtained for early stages ($Nt < 20$) and do not extrapolate simply to the late stages ($10 < Nt < 300$) measured here, as noted previously.

An exponent for the wake width can also be estimated as follows. If the velocity fluctuations have an exponent α_{u^*} and if the vorticity fluctuations have an exponent α_ω, the wake width should have an exponent $\alpha_{L_\omega} = \alpha_{u^*} - \alpha_\omega$ since the vorticity scales as $\omega \sim u/L$. This formula together with the measurements of α_{u^*} in (5.1) and α_ω in (5.2) leads to a value of the exponent for the wake width $\alpha_{L_\omega} = +0.21 \pm 0.03$, in good agreement with (5.5).

6. Asymmetric momentumless regime

This section focuses on the flow obtained when a slight angle of attack is present between the axis of the bluff body and the towing velocity. This configuration was first obtained unintentionally, but it revealed interesting features of the flow, and is

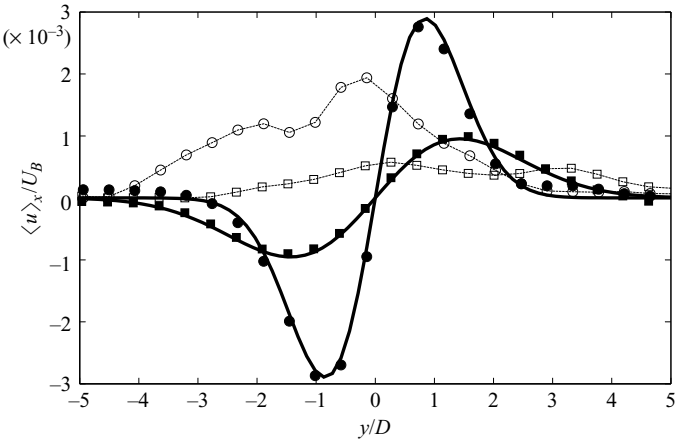

FIGURE 17. Profile of mean velocity (filled symbols) and quadratic fluctuations of velocity $u^* \equiv \langle u'^2 + v'^2 \rangle_x^{1/2}$ (open symbols) at times $Nt = 30$ (○) and $Nt = 200$ (□) for a spheroid with a slight angle of attack toward positive y. $F = 25$ and $Re = 16\,000$.

an example of the sensitive dependence on initial conditions that is a unique feature of the momentumless case.

As shown in figure 2(c), the vorticity fields obtained in the asymmetric regime are very organized, but differ from the ones obtained in the momentum regime (shown on figure 2a). The instantaneous vorticity fields contain three layers of vorticity in the asymmetric regime, whereas only two layers of vorticity are present in the momentum regime. In this experiment, the angle of attack was positive (toward the left), i.e. the nose of the bluff body was located at a small y^+. This leads to a layer of negative vorticity surrounded by two layers of positive vorticity. For such a distribution of vorticity, it can be deduced that the velocity profile must be asymmetric, as the data in figure 17 show. Although the angle of attack could not be measured accurately, it was estimated to be between 0.5° and 1°. The experiment was carried out for $U_B = U_C$, which means that the integral of the mean profile $\int U(y)\mathrm{d}y$ is equal to zero, as can be seen on figure 17. The towing velocity U_B had to be very close to the momentumless velocity for the profile to be asymmetric: a relative difference of 1% was sufficient to modify the profile from asymmetric to symmetric. In the asymmetric regime, the mean profile of velocity contains two lobes, a negative lobe of velocity for y^- and a positive lobe for y^+. This accords with the fact that the angle of attack is toward y^+: the propeller is located at a small y^-, and more fluid is expelled backwards at y^-, creating a negative velocity for y^-. On the other hand, for y^+, the jet of the propeller is weaker and more fluid is more entrained by the drag of the bluff body, creating a positive lobe of velocity for y^+.

Figure 17 also shows the quadratic fluctuations of velocity $u^* \equiv \langle u'^2 + v'^2 \rangle_x^{1/2}$ as open symbols. These fluctuations are slightly smaller than the mean profile, indicating that the wake may again be governed by the mean shear rather than by the turbulent fluctuations, as in the momentum regime. The measurements of the mean profile are clean enough and it is possible to fit the mean velocity by an odd function with an amplitude U_1 and a width L_1,

$$U(y) = U_1 \frac{y}{L_1} \mathrm{e}^{-y/2L_1^2}. \tag{6.1}$$

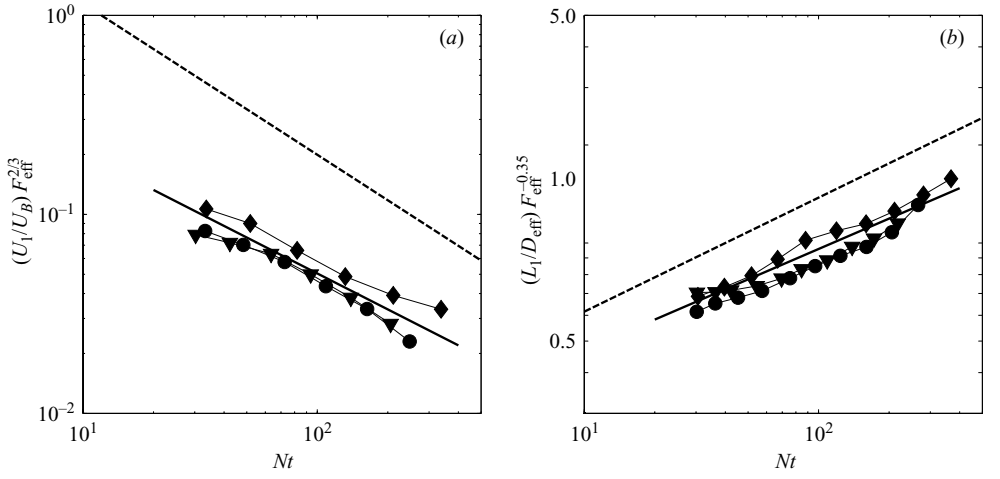

FIGURE 18. Amplitude (*a*) and wake width (*b*) of the mean profile of velocity for a spheroid with a Froude number $F = 25$ and $Re = 16\,000$.

This function is convenient because it is a self-similar solution of the diffusion equation $\partial U/\partial t = \nu_T \partial^2 U/\partial y^2$ which governs the wake in a non-stratified fluid. The fitting function is plotted in figure 17 as a solid line and shows a good fit to the experimental data, and hence a reasonable determination of the amplitude U_1 and the width L_1 of the wake as a function of time, which are plotted in figure 18 for three experiments in the same configuration (angle of attack, Froude number and Reynolds number).

The amplitude U_1 of the asymmetric mean profile is plotted in figure 18(*a*) and is compared with the prediction for a non-propelled bluff body given by equation (4.2), shown as a dashed line. The amplitude U_1 is four times weaker than in the non-propelled case, as expected since the experiments are conducted close to the momentumless velocity U_C and with a slight angle of attack. The amplitude should strongly depend on the angle of attack and it should vanish when the angle of attack vanishes. Hence, there was no attempt to predict the multiplying factor for the variation of U_1. However, it is possible that the scaling exponent may be universal in this regime, independent of the drag coefficient or the angle of attack. For this experiment, assuming the amplitude scales as $U_1 \sim Nt^{\alpha_{U_1}}$, the best fit (plotted as a solid line on figure 18*a*) is

$$\alpha_{U_1} = -0.6 \pm 0.06. \tag{6.2}$$

This value is smaller than the value $\alpha_U = -0.76$ found for momentum wakes, described in detail in § 4, but it is larger than the value $\alpha_{u^*} = -0.4$ found for the symmetric momentumless wakes, described in § 5. Further experiments would be required to confirm this result, and its possible dependence on Froude number and angle of attack.

Figure 18(*b*) shows the wake width normalized by the effective diameter. It is slightly smaller than in the case of a non-propelled wake, represented by the dashed line. This tendency was also obtained in the momentum regime – the propeller decreased the wake width (see figure 6*a*). However, in this case, it is not possible to use the momentum thickness $D_{\rm mom}$ defined by equation (4.3), since it is zero.

The wake width might be collapsed using a lengthscale based upon the (small but finite) angle of attack, but this was not feasible here since the angle of attack has not

been measured with sufficient precision. Nevertheless, assuming that the wake width scales as $L_1 \sim Nt^{\alpha_{L_1}}$, the scaling exponent of the wake width may yet be universal. A best fit of the results (shown as a solid line on figure 18*b*) gives

$$\alpha_{L_1} = +0.31 \pm 0.03, \tag{6.3}$$

which is indistinguishable from the value of $\alpha_L = +0.35$ obtained for momentum wakes but larger than the value of $\alpha_{L_\omega} = +0.18$ obtained for symmetric momentumless wakes.

To conclude, it seems that in the asymmetric momentumless regime, the scaling exponents are between the scaling exponents of the momentum regime and the scaling exponents of the momentumless regime. This may come from the fact that the mean profile of velocity is close to the quadratic fluctuations of velocity, meaning that the wake is governed by the mean shear but also by the turbulent fluctuations. This regime could be better analysed with a larger angle of attack and further experiments could be done in this regime, both on the grounds that a small angle of attack may not be that uncommon in practice and because the different balance between mean and turbulence-driven fluctuations might be instructive.

7. Discussion

7.1. *Momentumless wakes are not universal*

The true momentumless wake, where $|U_B - U_C| \leqslant 4\%$, has no coherent mean profile, and no obviously self-preserving form of the velocity fluctuations. The late-time wake decay exponents were found to depend on the initial conditions, as data for the cylinder with small and large propeller do not collapse. No drag wake, or any other case outside this particular limiting condition, has a measurable dependence on initial conditions in the late wake.

The lack of universal scaling laws in the momentumless wake is consistent with the observation that since, unlike drag wakes, there is no balance between turbulence production and dissipation, then turbulence parameters determined in near-wake initial conditions can continue to affect the far-wake similarity solutions (Finson 1975). It is also consistent with experimental observations in the literature for self-propelled bodies in non-stratified flows, showing measurable differences in the wakes of smooth and rough-walled bodies, and between wakes where the propulsion is provided by propellers or momentum jets (Swanson *et al.* 1974; Chieng *et al.* 1974; Higuchi & Kubota 1990; Sirviente & Patel 2000*a*, *b*).

It is important to note that this non-universality is measured here in the late wake. The data extend to $Nt = 500$ and $x/D = 10^4$ and appear to have reached their final, asymptotic state. There is experimental (e.g. Bevilaqua & Lykoudis 1978) and theoretical (Johansson *et al.* 2003) evidence showing that velocity fluctuations in particular may not reach a self-preserving form until far downstream, and many of the self-propelled results in the literature are for $x/D < 100$.

The ability of the current experiments to access and differentiate between almost and exactly self-propelled cases is due to the simultaneous operation of independent towing and thrust generation mechanisms. In this respect, the experiment is similar to that of Higuchi & Kubota (1990) where the thrust-producing central jet momentum flux was varied independently of the tunnel mean speed around a drag-producing body. In a similar systematic variation of the degree of propulsion, these authors also noted the unique characteristics of the precise self-propelled point.

The definition of momentumless here is different from other possible definitions, such as drag = thrust. Only the condition $\int_{-\infty}^{\infty}\langle u\rangle_x \mathrm{d}y = 0$ (equation (3.1)) is imposed and only at the horizontal centreplane. The fact that the self-propelled point defined this way ($U_B = U_C$) does lead to and correspond with a unique (almost singular in the sense of Finson 1975) flow field suggests that it is useful operationally, even if it does not account for all possible momentum fluxes (for example if surface or internal wave drag were significant; see next section).

7.2. *Momentumless wakes are unlikely*

The exact self-propelled point is rarely attained, because a number of conditions will pull the wake far enough away from it to enter a completely different regime. The possible perturbations include non-steady motion of the body, non-steady motion in the environment, and drag contributions from waves at boundaries, or (most likely in stratified flows) internally within the fluid.

The acceleration of a self-propelled body times its mass m is equal to the sum of the drag force and the thrust force. This can be rewritten, using the expressions for the drag force and the thrust force, as

$$m\frac{\mathrm{d}U_B}{\mathrm{d}t} = F_{\text{thrust}} - F_{\text{drag}} = c_D \tfrac{1}{2}\rho\left(U_C^2 - U_B^2\right)\frac{\pi D^2}{4}. \tag{7.1}$$

Here, U_B is the velocity of the bluff body and U_C is a velocity for which the momentum of the wake vanishes, proportional to the angular velocity of the propeller. When the bluff body reaches a constant speed, the acceleration is zero and the velocity of the bluff body equals the momentumless velocity U_C. The wake is thus in the momentumless regime. However, the time needed to reach this constant speed is infinite, and during the phase of acceleration, the wake will be better represented by the momentum regime.

We may estimate the time needed for the wake to reach the momentumless regime. By integrating the differential equation (7.1), the velocity U_B is governed by a law $U_B = U_C \tanh(t/\tau)$ with $\tau = 4L/c_D U_C$. For this result, the bluff body is assumed to be cylindrical, so that the mass m of the bluff body is equal to the density of the fluid ρ times the section of the bluff body $\pi D^2/4$ times the length L of the bluff body times a factor 2 to take into account the added mass. The velocity of the bluff body is thus equal to the momentumless velocity within 2% after a time $t = 2.3\tau$, which represents a distance close to $L_{\text{acc.phase}} \approx 1.6\tau U_C \approx 6.4L/c_D$. For example, a bluff body with a length of the order of 30 m leaves a momentum wake of a length close to one kilometre each time it changes the velocity of its propellers. It is only after this distance that the wake is in the momentum regime.

This calculation shows that the momentum regime may be representative of the wake of a real self-propelled body, if the velocity of the bluff body is not exactly constant. This is the case in the acceleration and deceleration phases. But it is also the case if the fluid has its own fluctuations of velocity, for example created by oceanic currents. If we assume that the length needed by the bluff body to reach its cruise velocity is much larger than the lengthscale of the currents, the bluff body will have a constant velocity and will experience variations in its momentumless velocity: the velocity of the currents is equal to the difference between the velocity of the bluff body U_B and the momentumless velocity U_C ($u_{\text{curr.}} = U_B - U_C$). Suppose the fluctuations $U_B - U_C$ are small compared to the velocity of the bluff body U_B, but big enough for the wake to be in the momentum regime. Then the mean absolute amplitude of the

wake can be obtained by taking the average of equation (4.5):

$$\langle |U_0| \rangle = 6.6(Nt)^{-0.76} F_{\text{eff}}^{-2/3} \frac{\langle |u_{\text{curr.}}|^{1/3} \rangle}{U_B^{1/3}} U_B. \tag{7.2}$$

If the fluctuations are of the order of 10% of the velocity of the bluff body, the mean absolute amplitude of the wake would be equal to 46% of the amplitude of the wake without a propeller. Thus, even if the fluctuations of velocity of the ambient fluid are small, the momentum can be high. We thus expect the wake to be in the momentum regime most of the time.

In the above analysis, the drag was imagined to be due only to the fluid entrained by the bluff body, as in a non-stratified fluid. However, in a stratified fluid, there is an additional drag due to the internal waves. This drag can be as high as 10% of the standard drag for Froude numbers between 2 and 10 (Lofquist & Purtell 1984). If $\lambda = F_{\text{int.waves}}/F_{\text{drag}}$ is the ratio between the drag due to the internal waves and the drag due to the entrained fluid, the thrust force can be calculated as $F_{\text{thrust}} = (1+\lambda)F_{\text{drag}}$ for a constant speed of the body. Since the internal waves propagate away very rapidly, the only momentum left in the wake at late stages is $J = F_{\text{drag}} - F_{\text{thrust}}$, which leads to a new definition of the momentum thickness,

$$D_{\text{mom}} = D\sqrt{\lambda c_D/2} = D_{\text{eff}}\sqrt{\lambda}. \tag{7.3}$$

The wake is now governed by the momentum created by the drag from the internal waves, in which case all the predictions made in § 4 remain valid if the momentum thickness is defined by (7.3). The value of the amplitude U_0 is easily found by introducing (7.3) into (4.4), so

$$\frac{U_0}{U_B} = -6.6(Nt)^{-0.76} F_{\text{eff}}^{-2/3} \lambda^{1/3}. \tag{7.4}$$

If the drag due to the internal waves is of the order of 10% of the drag due to the entrained fluid, the amplitude of the wake is still equal to 46% of the amplitude of the wake in the absence of the propeller. The stratified wake remains in the momentum regime even when the body is self-propelled, and moving at perfectly constant speed in a perfectly still environment.

8. Conclusions

Exactly momentumless wakes are very fragile and peculiar flows. They contain information from the initial conditions in the late wake: these include turbulence parameters, body/propeller geometry and angle of attack of the body. Unlike the drag wake, there is no single rescaling based only on wake momentum flux that will collapse measurements or predict, in a general way, the wake dynamics. In particular, the measurable turbulent fluctuations cannot be seen as being driven by some self-similar mean shear profile. This would bode ill for extrapolation of these kinds of results to practical applications, but for the fact that almost always some kind of momentum excess (positive or negative) will be present. That being the case, this paper establishes a set of universal scaling exponents that can be used to describe the mean flow, turbulence quantities and vortex geometry for all stratified (momentum) wakes, regardless of their origin. Some differences with literature results remain to be explained, but may be due in part to the difficulty of maintaining precise momentumless experiments, and partly to the fact that the experiments described

here apply to stages of the wake evolution that are an order of magnitude later than for other comparable data.

REFERENCES

Afanasyev, Y. D. 2004 Wakes behind towed and self-propelled bodies: Asymptotic theory. *Phys. Fluids* **16**, 3235–3238.

Bevilaqua, P. M. & Lykoudis, P. S. 1978 Turbulence memory in self-preserving wakes. *J. Fluid Mech.* **89**, 589–606.

Blevins, R. D. 1984 *Applied Fluid Dynamics Handbook*. Van Nostrand Reinhold.

Bonneton, P., Chomaz, J.-M. & Hopfinger, E. J. 1993 Internal waves produced by the turbulent wake of a sphere moving horizontally in a stratified fluid. *J. Fluid Mech.* **254**, 23–40.

Chernykh, G. G., Demenkov, A. G. & Kostomakha, V. A. 2001 Numerical modelling of a swirling turbulent wake behind a self-propelled body. *Russian J. Numer. Anal. Math. Model.* **16** (1), 19–32.

Chernykh, G. G., Ilyushin, B. B. & Voropayeva, O. F. 2003 Anisotropy decay of turbulence in a far momentumless wake in a linearly stratified medium. *Russian J. Numer. Anal. Math. Model.* **18** (2), 105–116.

Chieng, C. C., Jakubowski, A. K. & Schetz, J. A. 1974 Investigation of the turbulent properties of the wake behind self-propelled axisymmetric bodies. *VPI-Aero-025*. Virginia Polytechnic Institute, Blacksburg, Virginia.

Chomaz, J. M., Bonneton, P. & Hopfinger, E. J. 1993 The structure of the near wake of a sphere moving horizontally in a stratified fluid. *J. Fluid Mech.* **254**, 1–21.

Diamessis, P. J., Domaradzki, A. J. & Hesthaven, J. S. 2005 A spectral multidomain penalty method model for the simulation of high Reynolds number localized incompressible stratified turbulence. *J. Comput. Phys.* **202**, 298–322.

Dommermuth, D. G., Rottman, J. W., Innis, G. E. & Novikov, E. A. 2002 Numerical simulation of the wake of a towed sphere in a weakly stratified fluid. *J. Fluid Mech.* **473**, 83–101.

Fincham, A. M. & Spedding, G. R. 1997 Low-cost high-resolution dpiv for turbulent flows. *Exps. Fluids* **23**, 449–462.

Finson, M. L. 1975 Similarity behaviour of momentumless turbulent wakes. *J. Fluid Mech.* **71**, 465–479.

Gilreath, H. E. & Brandt, A. 1985 Experiments on the generation of internal waves in a stratified fluid. *AIAA J.* **23**, 693–700.

Gourlay, M. J., Arendt, S. C., Fritts, D. C. & Werne, J. 2001 Numerical modeling of initially turbulent wakes with net momentum. *Phys. Fluids* **13**, 3783–3802.

Hassid, S. 1980 Similarity and decay laws of momentumless wakes. *Phys. Fluids* **23**, 404–405.

Higuchi, H. & Kubota, T. 1990 Axisymmetric wakes behind a slender body including zero-momentum configurations. *Phys. Fluids* A **2**, 1615–1623.

Johansson, P. B. V., George, W. K. & Gourlay, M. J. 2003 Equilibrium similarity, effects of initial conditions and local Reynolds number on the axisymmetric wake. *Phys. Fluids* **15**, 603–617.

Lin, J. T. & Pao, Y. H. 1974 Turbulent wake of a self-propelled slender body in stratified and non-stratified fluids: analysis and flow visualizations. *APL/JHU POR-3586: Flow Research Rep. 11*.

Lin, J. T. & Pao, Y. H. 1979 Wakes in stratified fluids: a review. *Annu. Rev. Fluid Mech.* **11**, 317–338.

Lofquist, K. E. B. & Purtell, L. P. 1984 Drag on a sphere moving horizontally through a stratified liquid. *J. Fluid Mech.* **148**, 271–284.

Meunier, P. & Spedding, G. R. 2004 A loss of memory in stratified momentum wakes. *Phys. Fluids* **16**, 298–305.

Naudascher, E. 1965 Flow in the wake of self-propelled bodies and related sources of turbulence. *J. Fluid Mech.* **23**, 625–656.

Riley, J. R. & Lelong, M. P. 2000 Fluid motions in the presence of strong stable stratification. *Annu. Rev. Fluid Mech.* **32**, 613.

Schetz, J. A. & Jakubowski, A. K. 1975 Experimental study of the turbulent wake behind self-propelled slender bodies. *AIAA J.* **13**, 1568–1575.

Schooley, A. H. & Stewart, R. W. 1962 Experiments with a self-propelled body submerged in a fluid with vertical density gradient. *J. Fluid Mech.* **15**, 83–99.

Sirviente, A. I. & Patel, V. C. 1999 Experiments in the turbulent near wake of an axisymmetric body. *AIAA J.* **37**, 1670–1673.

Sirviente, A. I. & Patel, V. C. 2000*a* Wake of a self-propelled body, part 1: Momentumless wake. *AIAA J.* **38**, 611–619.

Sirviente, A. I. & Patel, V. C. 2000*b* Wake of a self-propelled body, part 2: Momentumless wake with swirl. *AIAA J.* **38**, 620–627.

Sirviente, A. I. & Patel, V. C. 2001 Turbulence in wake of a self-propelled body with and without swirl. *AIAA J.* **39**, 2411–2414.

Smirnov, S. A. & Voropayev, S. I. 2003 On the asymptotic theory of momentum/zero-momentum wakes. *Phys. Lett.* A **307**, 148–153.

Spedding, G. R. 1997 The evolution of initially turbulent bluff-body wakes at high internal froude number. *J. Fluid Mech.* **337**, 283–301.

Spedding, G. R. 2002 The streamwise spacing of adjacent coherent structures in stratified wakes. *Phys. Fluids* **14**, 3820–3828.

Spedding, G. R., Browand, F. K., Bell, R. & Chen, J. 2000 Internal waves from intermediate, or late-wake vortices. In *Stratified Flows I Proc. 5th Int. Symp. on Stratified Flows, Vancouver, Canada: UBC*. (ed. G. A. Lawrence, R. Pieters & N. Yonemitsu), pp. 113–118.

Spedding, G. R., Browand, F. K. & Fincham, A. M. 1996 Turbulence, similarity scaling and vortex geometry in the wake of a towed sphere in a stably stratified fluid. *J. Fluid Mech.* **314**, 53–103.

Swanson, R. C., Schetz, J. A. & Jakubowski, A. K. 1974 Turbulent wake behind slender bodies including self-propelled configurations. *VPI-Aero-024*. Virginia Polytechnic Institute, Blacksburg, Virginia.

Tennekes, H. & Lumley, J. L. 1972 *A First Course in Turbulence*. M.I.T. Press.

Voisin, B. 1991 Internal wave generation in uniformly stratified fluids. part 1. green's function and point sources. *J. Fluid Mech.* **231**, 439–480.

Voropayev, S. I. & Smirnov, S. A. 2003 Vortex streets generated by a moving momentum source in a stratified fluid. *Phys. Fluids* **15**, 618–624.